An Immune Cell Atlas Reveals Dynamic COVID-19 Specific Neutrophil Programming Amendable to Dexamethasone Therapy — Source link 🗗

Sarthak Sinha, Nicole L. Rosin, Rohit Arora, Elodie Labit ...+10 more authors

Institutions: University of Calgary, Alberta Children's Hospital

Published on: 19 Apr 2021 - bioRxiv (Cold Spring Harbor Laboratory)

Topics: ARDS, Innate immune system, Dexamethasone and Immune system

Related papers:

- Dexamethasone modulates immature neutrophils and interferon programming in severe COVID-19.

- A type I IFN, prothrombotic hyperinflammatory neutrophil signature is distinct for COVID-19 ARDS

- COVID-19 ARDS is characterized by a dysregulated host response that differs from cytokine storm and is modified by dexamethasone

- Neutrophils mediate Th17 promotion in COVID-19 patients.

- Innate immune deficiencies in patients with COVID-19

1   **An Immune Cell Atlas Reveals Dynamic COVID-19 Specific Neutrophil Programming Amenable to**

2   **Dexamethasone Therapy**

3   **Authors:** Sarthak Sinha[1*], Nicole L. Rosin[1*+], Rohit Arora[1], Elodie Labit[1], Arzina Jaffer[1], Leslie Cao[1],

4   Raquel Farias[3,4], Angela P. Nguyen[3,4], Luiz G. N. de Almeida[2,5], Antoine Dufour[2,5], Amy Bromley[6],

5   Braedon McDonald[3,4], Mark Gillrie[3,7,8], Marvin J. Fritzler[3,8], Bryan Yipp[3,4 +], Jeff Biernaskie[1,9,10 +]

6   **Affiliations:**

7   [1] Department of Comparative Biology and Experimental Medicine, Faculty of Veterinary Medicine,

8   University of Calgary;

9   [2] Department of Physiology & Pharmacology;

10   [3] Calvin, Phoebe and Joan Snyder Institute for Chronic Diseases, Cumming School of Medicine,

11   University of Calgary;

12   [4] Department of Critical Care Medicine, Cumming School of Medicine, University of Calgary;

13   [5] McCaig Institute for Bone and Joint Health, University of Calgary;

14   [6] Department of Pathology and Laboratory Medicine, University of Calgary;

15   [7] Department of Microbiology, Immunology and Infectious Diseases, University of Calgary;

16   [8] Department of Medicine, Cumming School of Medicine, University of Calgary, Calgary, AB, Canada;

17   [9] Hotchkiss Brain Institute, University of Calgary;

18   [10] Alberta Children's Hospital Research Institute, University of Calgary

19   [*] Equal contribution

20   [+] Corresponding authors

21

22   **Summary**

23   SARS-CoV-2 is a novel coronavirus that causes acute respiratory distress syndrome (ARDS), death and

24   long-term sequelae. Innate immune cells are critical for host defense but are also the primary drivers of

25   ARDS. The relationships between innate cellular responses in ARDS resulting from COVID-19

26   compared to other causes of ARDS, such as bacterial sepsis is unclear. Moreover, the beneficial effects of

27   dexamethasone therapy during severe COVID-19 remain speculative, but understanding the mechanistic

28   effects could improve evidence-based therapeutic interventions. To interrogate these relationships, we

29   developed an scRNA-Seq and plasma proteomics atlas (biernaskielab.ca/COVID_neutrophil). We

30   discovered that compared to bacterial ARDS, COVID-19 was associated with distinct neutrophil

31   polarization characterized by either interferon (IFN) or prostaglandin (PG) active states. Neutrophils from

32   bacterial ARDS had higher expression of antibacterial molecules such as PLAC8 and CD83.

33   Dexamethasone therapy in COVID patients rapidly altered the IFN^{active} state, downregulated interferon

34   responsive genes, and activated IL1R2^{+ve} neutrophils. Dexamethasone also induced the emergence of

35   immature neutrophils expressing immunosuppressive molecules ARG1 and ANXA1, which were not

36   present in healthy controls. Moreover, dexamethasone remodeled global cellular interactions by changing

37   neutrophils from information receivers into information providers. Importantly, male patients had higher

38   proportions of IFN^{active} neutrophils, a greater degree of steroid-induced immature neutrophil expansion,

39   and increased mortality benefit compared to females in the dexamethasone era. Indeed, the highest

40   proportion of IFN^{active} neutrophils was associated with mortality. These results define neutrophil states

41   unique to COVID-19 when contextualized to other life-threatening infections, thereby enhancing the

42   relevance of our findings at the bedside. Furthermore, the molecular benefits of dexamethasone therapy

43   are also defined, and the identified pathways and plasma proteins can now be targeted to develop

44   improved therapeutics.

45

46

2

47   **COVID-19 ARDS host responses contextualized to bacterial ARDS.**

48   A broad array of infections including SARS-CoV-2 and bacterial sepsis can induce acute respiratory

49   distress syndrome (ARDS), respiratory failure and death[1-3]. Neutrophils are thought to be key drivers of

50   both COVID-19 and bacterial ARDS[4-6], yet it is unclear if this is related to intrinsic and/or irreversible

51   cellular responses. While recent studies have leveraged single-cell transcriptomics to dissect peripheral[7-

52   9]and bronchoalveolar fluid [10-12]immune landscapes driving COVID-19 pathogenesis, the protocols used

53   can inadvertently exclude the majority of polymorphonuclear granulocytes, including neutrophils, as they

54   are highly sensitive cells with low RNA (and high RNase) content. Here, we employ whole-blood-

55   preserving protocols that capture all major immune cell types from critically ill patients admitted to

56   intensive care units (ICUs) (Extended Fig 1). All samples taken from COVID-19 patients were assessed

57   by bacterial culture and tested negative. All COVID-19 patients tested positive by PCR for SARS-CoV-2,

58   and we previously confirmed an absence of viral mRNA in any circulating immune cells in a subset of

59   patients[13]. However, a plasma proteomic screen for SARS-CoV-2 specific viral proteins in all samples

60   revealed detection of one or more viral proteins in COVID-19 patient serum (Extended Fig 2a).

61   Furthermore, we compared patient samples from COVID-19 ARDS to bacterial sepsis with ARDS

62   (herein referred to as bacterial ARDS) (Extended Fig 2b), as there were unusually low admissions to ICU

63   with viral pneumonias/ARDS during the period studied, likely due to COVID-19 public health measures.

64   Patient cohorts had comparable ages, sex, days on life support and time in hospital, but COVID-19

65   patients had broader racial diversity (Extended Fig 2c,d, Extended Data Table 1). Bacterial ARDS

66   induced significant neutrophilia, and relative thrombocytopenia compared to the near normal circulating

67   neutrophil numbers in COVID-19, while both had similar degrees of lymphopenia (Extended Fig 2e).

68   Both cohorts had comparable PaO2 / FiO2 (P/F) ratios, which is an indicator of the severity of ARDS[14],

69   but bacterial ARDS patients had significantly more kidney injury demonstrated by higher levels of serum

70   creatinine (Extended Fig 2f). We further compared families of soluble inflammatory markers (Extended

71   Fig 2g) used to distinguish prototypical states, including those identified during cytokine storm (Extended

72   Fig 2h) and cytokine release syndrome (Extended Fig 2i)[15], which demonstrated similar soluble cytokine

73   and chemokine responses between the infections. Therefore, in the context of life-threatening bacterial

74   ARDS, COVID-19 ARDS patients had normal neutrophil counts, comparable IL-6 levels, and less organ

75   failure as indicated by serum creatinine levels, all of which have been previously proposed as markers of

76   COVID disease severity[16,17]. This prompted us to further investigate immune states and composition in

77   response to COVID-19 compared to bacterial ARDS.

78   The online companion atlas (biernaskielab.ca/COVID_neutrophil) contains accessible scRNAseq data

79   performed on freshly obtained whole blood at timepoint 1 (t1, <72h after ICU admission) and at timepoint

80   2 (t2, 7 days after t1) (Fig 1a). Cellular identity was mapped to 30 immune cell types/states using a

81   UMAP projection from 21 patients and 86,935 cells (Fig 1b, Extended Figure 3a). Global magnitude of

82   gene expression was directly compared between COVID-19 and bacterial ARDS patients (Extended Data

83   Table 3), which revealed a more globally altered distribution of differential expression at t1 than at t2.

84   Altered regulation of genes was most pronounced in neutrophils at t1, with lower neutrophil gene

85   expression in COVID-19 compared to bacterial ARDS (Fig 1c; Extended Fig 3b-c). At t2, the global

86   alterations in gene expression when comparing COVID-19 to bacterial ARDS were most pronounced in

87   plasmablasts (Fig 1d; Extended Fig 3d-e). We further compared and quantified the proportions of known

88   peripheral blood cellular constituents, which highlighted significant differences in CD4 T cells, CD8 T

89   cells and NK cells (Extended Fig 3f). These data highlight that significant global differences in immune

90   cell gene expression exist between COVID-19 ARDS and bacterial ARDS.

91   **COVID-19 drives specific neutrophil maturation states.**

92   Neutrophils are a primary participant in the development of ARDS[18]; yet despite similar severity of

93   ARDS between our bacterial and COVID-19 cohorts, the numbers of circulating neutrophils from clinical

94   cell counts were significantly different (Extended Fig 2d). We hypothesized that neutrophil qualitative

95   states may be important determinants of disease. Neutrophils were subjected to velocity analysis[19,20] to

96   reconstruct maturation dynamics. Louvain clusters (Fig 1e), clinical cohort, individual patient, and

4

97   velocity length were overlayed on velocity vector fields (Extended Fig 4a-d). The proportions of distinct

98   neutrophil states were compared at t1 and this revealed a divergent expansion of IFN^{active} neutrophils

99   (clusters 2, 4 and 5) marked by IFITM1 expression in COVID-19, which became similar to bacterial

100   ARDS at t7 (Fig 1f-h). Expression of IFITM1 in neutrophils from COVID-19 patients at t1 was

101   confirmed by immunofluorescent staining for IFITM1, colocalized with S100A8/9 and typical neutrophil

102   nuclear morphology. Relative to healthy donors, the IFN^{active} population in both COVID-19 and bacterial

103   ARDS patients were elevated (Extended Fig 4h-k), suggesting that infections dramatically alter neutrophil

104   dynamics and that comparing COVID-19 neutrophils to healthy neutrophils may only reveal broad

105   features separating pathogen-challenged versus non-challenged (homeostatic) neutrophils. Hence, to map

106   pathogen-activated neutrophils dynamics with high resolution, subsequent analyses employ principal

107   components with top loading genes that distinguish different pathogen-activated states arising during

108   COVID-19 and bacterial sepsis for downstream dimensionality reduction.
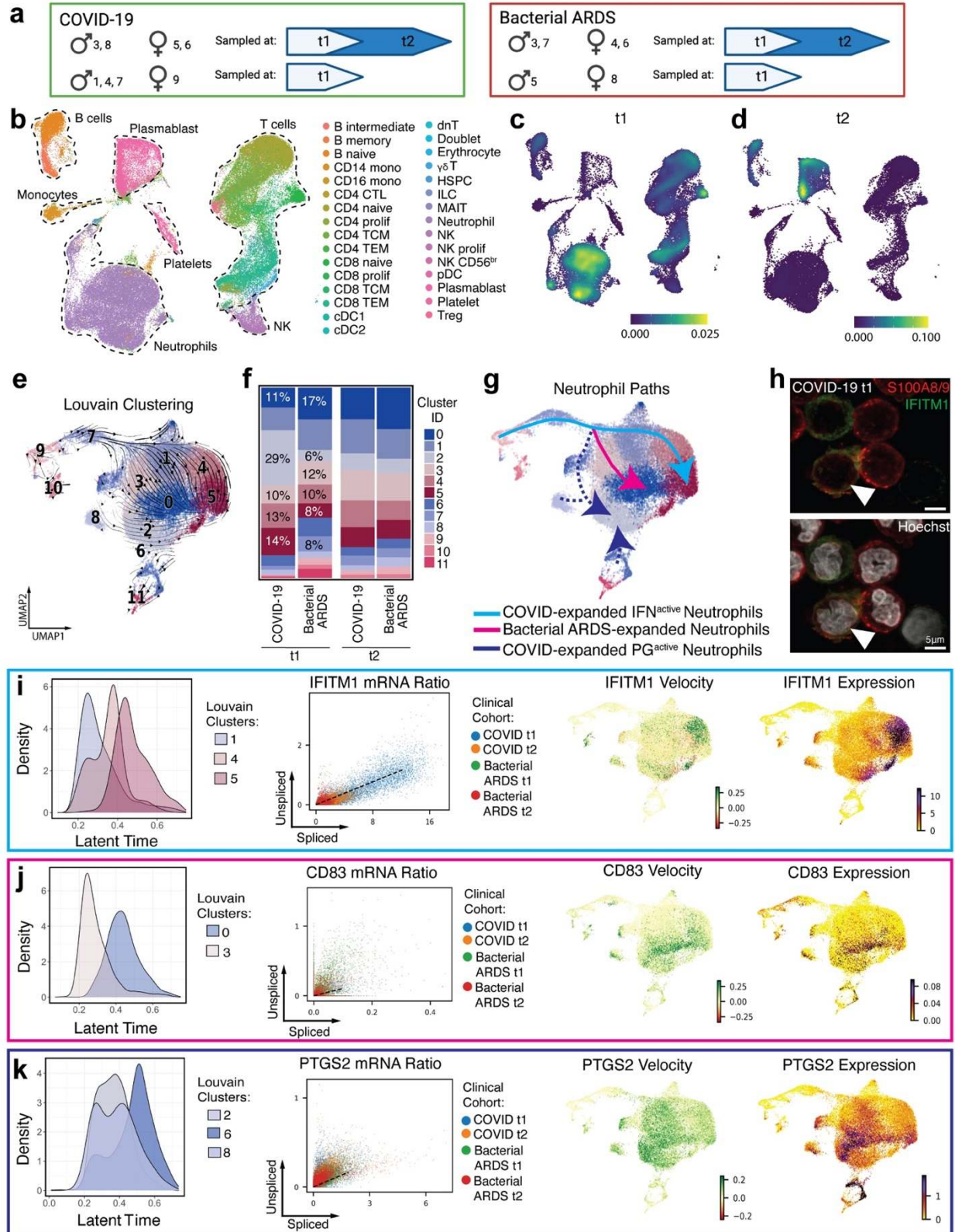
109

110 **Figure 1 – COVID-19 alters neutrophil maturation. a.** Schematic summarizing patients with COVID-
111 19 and bacterial sepsis profiled at t1 and t2. **b.** UMAP projection of 86,935 whole blood cells from 21

112 patient samples, coloured by Azimuth reference-mapped immune cell states. **c-d.** Kernel density estimates
113 depicting magnitude of molecular response elicited by immune cell subsets during COVID-19 compared
114 to Bacterial ARDS at t1 (c) and t2 (d) calculated by summing DEG fold changes for each cell state shown
115 in Panel a. **e.** UMAP plotting RNA velocity analysis of 29,653 subclustered neutrophils undergoing state
116 transitions, coloured by cluster ID. **f.** Stacked bar plot depicting cluster composition of clinical cohorts
117 examined. **g.** UMAP coloured by neutrophil clusters and overlaid with summary path curves based on
118 vector fields and neutrophil state compositions in Panel d and e, respectively to determine neutrophil
119 states. **h.** Immunocytochemistry for S100A8/A9 (red) and IFITM1 (green) expression on leukocyte-rich
120 preparation from COVID-19 donor at tl. **i-k.** Transcriptional kinetics driving expansion of IFN^{active} (i),
121 Bacterial ARDS-enriched (j), and PG^{active} (k) neutrophils. Latent time distribution of trajectory-associated
122 louvain clusters (left), phase portraits with equilibrium slopes of spliced–unspliced ratios (center), and
123 RNA velocity and gene expression (right) of selected genes driving divergent maturation trajectories.
124 Phase portraits are coloured by clinical cohort.

125 Classically, peripheral neutrophils are considered terminally differentiated and non-dividing, however the

126 increase in velocity length suggested the ability to alter phenotypic states once in circulation along

127 specific paths or 'lineages'. COVID-19 neutrophils followed unique maturation paths compared to

128 bacterial ARDS, culminating in three distinct terminal states: Interferon active (IFN^{active}), prostaglandin

129 active (PG^{active}) or bacterial ARDS enriched (Fig 1e-g; Extended Fig 4e). Interestingly, the apex of this

130 trajectory was marked by high velocity lengths, characteristic of cells undergoing differentiation

131 (Extended Fig 4c, d). COVID-19 neutrophils preferentially transitioned from the apex of the trajectory,

132 which was an immature state (TOP2A expressing; Extended Fig 4e) to an IFN responsive state

133 characterized by IFITM1, IFITM2 and IFI6 expression (Cluster 1 to 4 and 5; Fig 1i; Online Atlas). This is

134 clearly illustrated in Extended Video 1. This immature state was not present in healthy controls, though it

135 is present in both comparator groups, suggesting these states are liberated into circulation upon pathogen

136 exposure (Extended Fig 4h-k). The lineage relationship was less clear for COVID-19 enriched PG^{active}

137 clusters defined by prostaglandin responsive genes (clusters 2, 6 and 8), with notable increases in

138 PTGER4 and PTGS2 (or COX2), a proposed therapeutic target in COVID-19[21] (Fig 1k; Extended Fig 4f,

139 g, Online Atlas). The dominant conventional bacterial ARDS state was characterized by antibacterial

140 proteins CD83[22], CD177, and PLAC8[23] (cluster 3 to 0; Fig 1j; Online Atlas). Taken together, this data

141 demonstrated that peripheral neutrophils have dynamic programming abilities which result in COVID-19

142 specific neutrophil polarization defined by the emergence of IFN^{active} and PG^{active} neutrophil states.

7

143 **Unique transcriptional regulatory pathways drive neutrophil maturation in COVID-19.**

144 Rapid and robust IFN responses protect against COVID-19 severe disease, while delayed responses could

145 exacerbate systemic and pulmonary inflammation[24,25]. Moreover, neutrophil IFN responses are not

146 traditionally considered during infections and neutrophils are generally considered to be homogenous,

147 with a uniform proinflammatory capacity. Global neutrophil expression aligned with neutrophil state

148 specific markers, such as interferon response genes (IFITM1, RSAD2, IFI6, and ISG10), being more

149 highly expressed in COVID-19 neutrophils (Fig 2a; Extended Fig 4f). The inverse was the case for anti-

150 bacterial proteins like PLAC8 (Fig 2a; Online Atlas). However, the discovery of differential neutrophil

151 states prompted further exploration of the factors driving neutrophil state polarization. Gene regulatory

152 network reconstruction using SCENIC analysis[26] revealed differentially activated transcription factors

153 STAT1, IRF2 and PRDM1 in COVID-19 (Fig 2b), while bacterial ARDS neutrophils had increased

154 prototypical granulocyte transcription factors such as CEBPA, CEBPB, STAT5B and less defined factors

155 such as NFE2 (Fig 2b, Online Atlas). PRDM1 activation was most pronounced in the IFN^{active} neutrophil

156 population and was likely responsible for driving expression of interferon response elements (IFIT1,

157 ISG15, IFI6) and antiviral signaling, such as RSAD2 and STAT1 (Fig 2c; Online Atlas). A hallmark of

158 PG^{active} neutrophil polarization was the activation of an E2F4 pathway (Fig 2d), while neutrophil

159 programming during bacterial ARDS included STAT5B (Fig 2e). To summarize, in response to COVID-

160 19, neutrophils were polarized by unique transcriptional regulation towards one of two main populations,

161 either an IFN^{active} population or a PG^{active} population (Fig 2f).

162
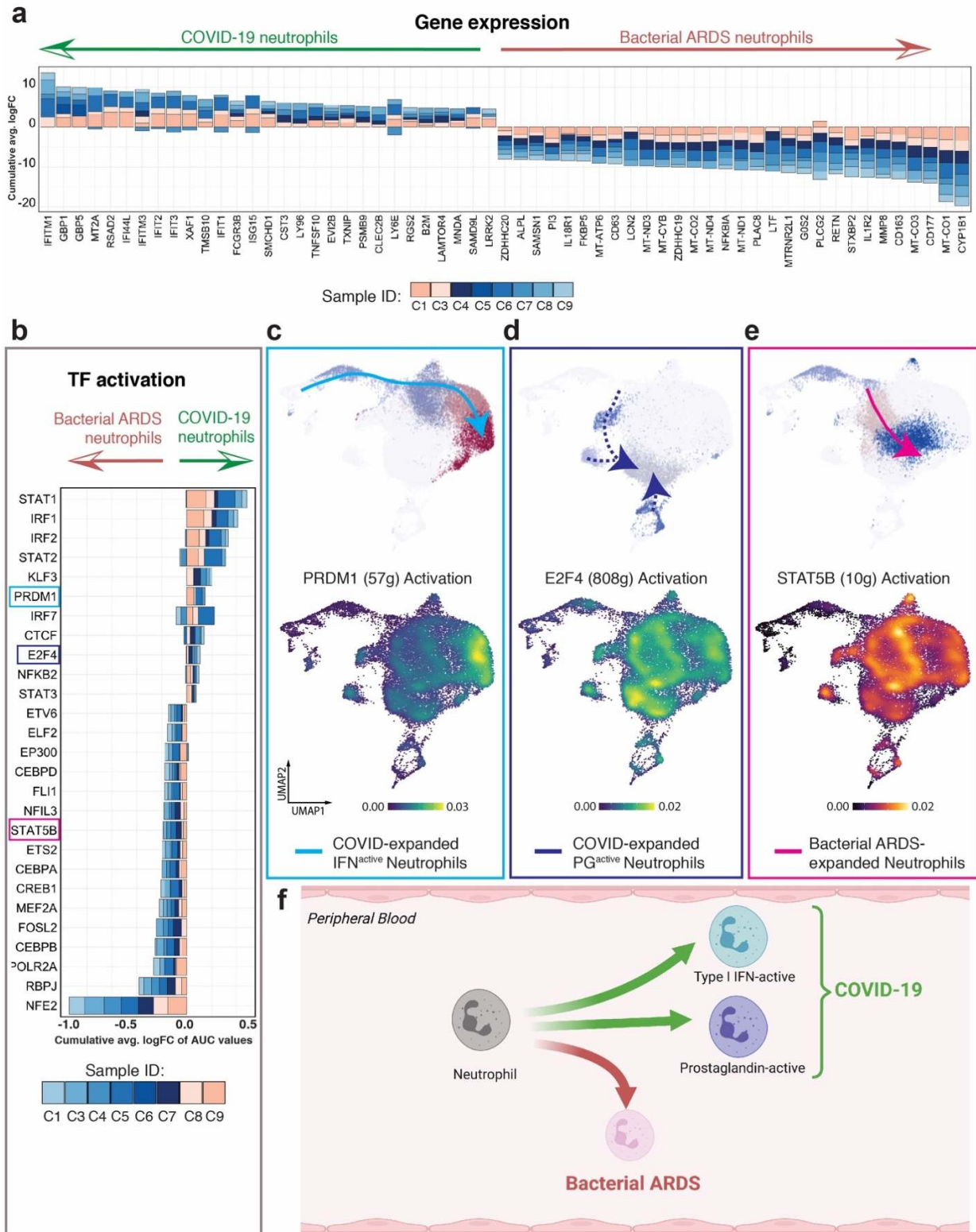
Figure 2 – Distinct regulatory programs drive divergent neutrophil maturation. a. Consensus neutrophil DEGs upregulated (positive FC) or suppressed (negative FC) during COVID-19 in at least 3 of 8 patients at t1 relative to Bacterial ARDS. **b.** Differentially activated consensus transcription factors

166   (TFs) in neutrophils from patients with COVID-19 relative to bacterial ARDS at t1. Stacked bars depict

167   logFC contributions of each COVID-19 patient. **c-e.** Gene-regulatory networks preferentially driving

168   IFN^{active} (PRDM1, c), PG^{active} (E2F4, d), and bacterial ARDS-enriched (STAT5B, e) neutrophil states.

169   Scale bars depict kernel density estimates approximating magnitude of TF activation inferred by

170   SCENIC-calculated AUCell scores. **f.** Schematic summarizing neutrophil fates favoured during COVID-

171   19 versus bacterial ARDS.

172

173   **Dexamethasone alters immune cell dynamics and plasma proteomic milieu.**

174   Conventional therapeutics have limited efficacy for COVID-19, and while dexamethasone offers a

175   moderate benefit, the RECOVERY trial reported the benefit was greatest in the most severely affected

176   patients[27]. However, the mechanisms underlying this benefit are unclear and not universal, so opportunity

177   exists to optimize or better target this therapy. In our cohort, median time between dexamethasone

178   administration to t1 blood draw (within 72 hours of ICU admission) was 31 hours (Fig 3a, Extended

179   Figure 5a, Extended Table 1). Global differences in transcription were apparent at t1 with clear

180   upregulation of genes in neutrophils and some T cell subsets in COVID-19 patients treated with

181   dexamethasone versus those that were not treated (Fig 3b-d, Extended Figure 5b, Extended Data Table 4).

182   Dexamethasone globally downregulated genes at t1, including in naïve B cells, plasmablasts and some T

183   cells (Extended Figure 5b-d). At t2 gene upregulation occurred in adaptive immune cells, including naïve

184   and effector CD8 T cells, with limited alterations in the innate myeloid cell lineages including

185   neutrophils. However, neutrophils demonstrated clear down regulation of genes at t2, as did CD4 naïve

186   and central memory T cells (Extended Figure 5e, f). Proportionally, at t1, dexamethasone administration

187   was associated with an increase in cytotoxic CD4 T cells, naïve B cells, plasmablasts, and decreased

188   proliferating NK cells, and CD4 effector memory cells (Extended Fig 5g). By t2, dexamethasone was

189   associated with suppressed neutrophil proportions in circulation compared to untreated controls (13% vs

190   41%, Extended Fig 5g). Plasma proteomics from the same cohort revealed that dexamethasone

191   suppressed 10 host proteins (S100A8, S100A9, SERPINA1, SERPINA3, ORM1, LBP, VWF, PIGR,

192   AZGP1, CRP) that others have previously identified as biomarkers distinguishing severe COVID-19

193   cases from mild to moderate counterparts (full host proteome quarriable via Online Atlas; Extended Table

10

194   2)[28-31]. Suppression of calprotectin (S100A8/S100A9) and neutrophil serine proteases (SERPINA1 and

195   SERPINA3), paired with depletion of neutrophil proportions, implicates the modulation of neutrophil-

196   related inflammatory processes as a method of action for dexamethasone treatment.

197

12
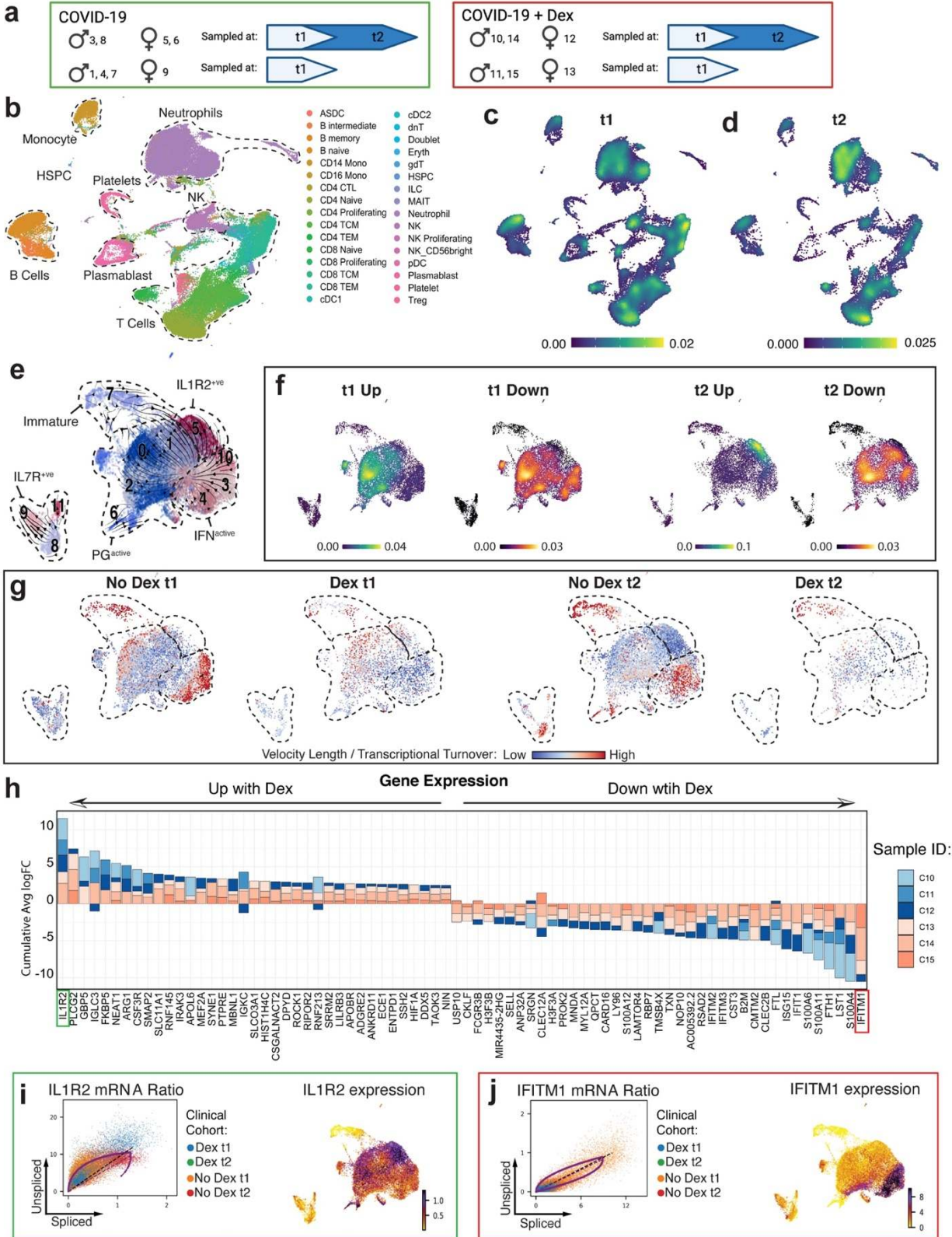
198 **Figure 3 – Dexamethasone suppresses IFN programs and depletes IFN**[active] **neutrophils in COVID-**
199 **19. a.** Schematic summarizing COVID-19 patients treated with or without dexamethasone profiled at t1
200 and t2. **b.** UMAP projection of 80,994 whole blood cells from 21 patient samples, coloured by Azimuth
201 reference-mapped immune cell states. **c-d.** Kernel density estimates depicting magnitude of molecular
202 response elicited by immune cell subsets following Dexamethasone treatment t1 (c) and t2 (d) calculated
203 by summing DEG fold changes for each cell state shown in Panel A. **e.** Neutrophil states overlaid on a
204 UMAP of 23,193 subclustered neutrophils from Dexamethasone- and non-Dexamethasone-treated
205 COVID-19 patients, colored by cluster ID. **f.** Magnitude of molecular response elicited by each neutrophil
206 state post-Dexamethasone treatment calculated by summing DEG fold changes for each cell state shown
207 in Panel d. **g.** RNA velocity vector length (indicating rate of differentiation/state transition) in
208 Dexamethasone- and non-Dexamethasone-treated neutrophils at t1 and t2. **h.** Consensus neutrophil DEGs
209 upregulated (positive FC) or suppressed (negative FC) post-Dexamethasone in at least 3 of 6 COVID-19
210 patients at t1 relative to non-Dexamethasone COVID-19 controls. Stacked bars depict logFC contribution
211 of each Dexamethasone-treated patient. **i-j.** Differential splicing kinetics drives activation of IL1R2 (i)
212 and suppression of IFITM1 expression (j) post-Dexamethasone treatment. Phase portraits show
213 equilibrium slopes of spliced–unspliced mRNA ratios. Green denotes most upregulated and red denotes
214 most down regulated differentially expressed genes with COVID-19 (f).

215

216 **Dexamethasone therapy restrains neutrophil IFN programs**

217 Due to the early and sustained effects of dexamethasone on gene expression in neutrophils, the effects of

218 dexamethasone therapy on neutrophil functional states were evaluated. Neutrophil reclustering again

219 identified immature neutrophils at the apex of the maturation trajectory, accelerating and exhibiting

220 maximal divergence prior to PG[active] and IFN[active] state commitments (Fig. 3 d, Extended Fig 6a-e).

221 Interestingly, we also identified IL7R[+ve] neutrophils (comprising roughly 8% of total neutrophils) whose

222 trajectories remained completely separate (Fig. 3 d, Extended Fig 6g, j) suggesting an entirely distinct

223 neutrophil state. Initially, dexamethasone was associated with increased global transcription in PG[active]

224 neutrophils, while ongoing therapy resulted in the emergence of a PG[active] neutrophils concomitant with

225 high IL1R2 expression (IL1R2[+ve]) (Fig. 3 e). Conversely, dexamethasone had a pronounced attenuation of

226 global transcription of IFN[active] neutrophils at t1 and t2 (Fig 3 e, f). Remarkably, dexamethasone

227 administration at t1 halted dynamic state changes in IFN[active] and IL7R[+ve] neutrophils, followed by

228 preferential depletion of IFN[active] subsets (Fig 3 g). Indeed, dexamethasone was associated with a

229 reduction in IFN[active] neutrophils to a proportion more similar to that detected in healthy controls (9%

230 post-Dex at t2 versus 10% in healthy controls) (Fig. 4a, Extended Fig 4h-k). Although collection of

231 airway samples (i.e. bronchoalveolar lavage fluid; BALF) was not feasible at our institution, we leveraged

13

232   two recent BALF scRNA-Seq datasets[11,32] to assess whether IFN^{active} neutrophils dominate the

233   bronchoalveolar landscape during severe COVID-19. Projection of CSF3R$^+$S100A8$^+$S100A9$^+$ BALF

234   neutrophils onto our reference revealed: a. 1.5 FC expansion of IFN^{active} neutrophils in severe COVID-19

235   relative to moderate disease (77% vs 52%, Extended Fig 7a-b), b. preferential activation of IFN-

236   stimulated genes such as IFITM1, IFITM2, IFI6, IRF7, and ISG20 in severe COVID-19 neutrophils

237   (Extended Fig 7c), and c. 4.7 FC greater IFN^{active} neutrophils in COVID-19 relative to bacterial

238   pneumonia patients (14% vs 3%, Extended Fig 7d-f). Albeit anecdotal, in our whole blood cohort, the

239   IFN^{active} neutrophil state was dominant in patient S7 [32], an 80-year-old male with remarkably high viral

240   titers who succumbed to COVID-19 complications within 3-4 days of sampling (Extended Fig 7f).

241   Consensus DEG analysis highlighted that upregulation of IL1R2, a decoy receptor that sequesters IL-1,

242   and downregulation of IFITM1 were the most prominent discriminating features of treatment with

243   steroids (Fig. 3h). Additionally, dexamethasone attenuated neutrophil expression of IFN pathways more

244   broadly, including the reduction of IFITM1-3, IFIT1, ISG15 and RSAD2 (Fig 3h). Examination of

245   unspliced pre-mRNA to mature spliced mRNA ratios supported the notion that induction of

246   immunoregulatory systems (i.e., IL-1R2; Fig 3 i) and suppression of IFN (i.e., IFITM1; Fig 3 j) programs

247   were driven by differential splicing kinetics.

248   **Dexamethasone therapy intensifies neutrophil immunosuppressive function**

249   Corticosteroid therapy shifted neutrophil state compositions. While IFN^{active} neutrophils were significantly

250   depleted by seven days of therapy, there was >2-fold expansion in immature neutrophils relative to non-

251   treated COVID-19 controls (Fig 4a; Extended Fig 6 h, i), which were absent in the healthy controls.

252   Albeit anecdotal, the dominance of IFN^{active} neutrophils at t1 in the patient who succumbed to COVID-19

253   in the non-dexamethasone cohort further supports depletion of IFN^{active} neutrophils as a mechanism by

254   which dexamethasone is protective (Extended Fig 8 g-j). Assessment of gene regulatory networks

255   demonstrated that IRF7 and MEF2A exhibited opposing activation patterns, with IRF7 being the most

256   suppressed and MEF2A the most enhanced transcription factors identified with dexamethasone, which

14

257 correlates with the emergence of PG^{active} and IL1R2^{+ve} states and attenuation of the IFN^{active} neutrophil

258 states (Fig 4b, Extended Fig 6k-m). To assess the generalizability of the dexamethasone regulated DEGs

259 identified in our cohort, we asked whether they accurately predicted mortality due to COVID-19 in a

260 larger validation cohort. By leveraging a whole blood bulk RNA-Seq dataset from 103 COVID-19

261 patients[33 34], we scored each sample by the aggregated expression of dexamethasone suppressed DEGs at

262 t1 and t2 (Extended Data Table 3). Interestingly, suppressed DEGs at t2 (but not t1) proved to be a far

263 superior predictor of 28-day mortality (AUC: 0.78, CI: 0.67 -0.89) compared to clinical severity scales

264 such as sequential organ failure assessment (SOFA) (AUC: 0.67, CI: 0.51-0.82) across all classification

265 thresholds (Fig 4c).

266 Unexpectedly, steroid administration was associated with an increase in circulating immature neutrophils,

267 which highly expressed TOP2A, and activated ATF4 and JDP2, transcription factors seen in

268 undifferentiated cells or those undergoing nuclear reprogramming (Extended Fig 6h). Interestingly, these

269 immature neutrophils expressed high levels of ARG1, ANXA1 (Fig 4d), and CD24 (both mRNA and

270 protein; Extended Fig 6 i), also suggesting an immunomodulatory role[35,36,37-39] that was expanded with

271 dexamethasone treatment. Both ARG1 and ANXA1 express glucocorticoid response elements, supporting

272 direct regulation by dexamethasone treatment[40,41].

273 To further understand the role of neutrophils during COVID-19 and the effects of dexamethasone, we

274 investigated cellular connectomes. Cellular interactions between many cell types (including highly

275 interactive neutrophils) were noted (Extended Fig 8a), and dexamethasone altered the globally predicted

276 interactions by suppressing intercellular signalling, in both number and strength of interactions (Extended

277 Fig 8b, c). Dexamethasone enhanced (Fig 4e) and suppressed (Extended Fig 8d) a number of unique

278 neutrophil-driven signalling networks. Of note, annexin family signalling, which was enhanced in the

279 immature neutrophils and represent powerful immunomodulators, were augmented between neutrophils

280 and the other circulating immune cells when patients received dexamethasone (Fig 4e). Of note is the

281 direction of annexin family signaling, which switched from incoming toward neutrophils without

15

282   dexamethasone treatment to being almost entirely outgoing from neutrophils toward B intermediate and

283   memory cells and MAIT cells following dexamethasone (Fig 4f, g, Extended Fig 8e, f). Therefore,

284   dexamethasone directly altered neutrophil functional states, by promoting expansion of an

285   ARG1+/ANXA1+ immature state with immunosuppressive features and altered the global

286   communication structure such that neutrophils became active instructors of some peripheral immune

287   cells.

Neutrophil response to dexamethasone is sexually dimorphic

289   Given the apparent clinical benefit of dexamethasone is more evident in males[27], and since males are

290   predisposed to more severe COVID-19 presentations and outcomes[42] , we surmised that dexamethasone

291   incites sexually dimorphic immunosuppressive effects. Our retrospective province-wide audit comparing

292   72 pre-dexamethasone (51 M, 21 F) versus 1,581 post-dexamethasone (1013 M, 568 F) treated ICU-

293   admitted patients confirmed a preferential mortality benefit in male COVID-19 patients (Extended Fig 9a,

294   b). While dexamethasone modulated 525 neutrophil DEGs across both sexes, while 892 were uniquely

295   modulated in either males or females (Extended Data Table 5). Amongst the jointly modulated DEGs, a

296   subset (24 of 525) exhibited statistically significant dimorphism in either magnitude or direction of

297   regulation (Extended Fig 9c, d). Interestingly, while neutrophils were depleted in both sexes post-

298   dexamethasone, this was particularly pronounced in males (1.9 FC higher in males at t1 and 3.4 FC

299   higher in males at t2, Extended Fig 9e). Of the two salient neutrophil state alterations, an immature

300   (ARG1^{+ve} immunosuppressive) state was preferentially expanded with dexamethasone in males (Extended

301   Fig. 9e), whereas ISGs were preferentially suppressed (Extended Fig. 9f) and IFN^{active} states were

302   depleted in females (Extended Fig. 9g-h) at both t1 and t2 (Fig 4h, i). Sexually dimorphic effects of

303   dexamethasone on neutrophil maturation kinetics may in part explain these state alterations. Dynamo-

304   reconstructed vector dynamics revealed that dexamethasone slowed IFN^{active} transitions (Extended Fig. 9i)

305   whilst accelerating immature (ARG1^{+ve} immunosuppressive) neutrophil differentiation in females

306   (Extended Fig. 9j) ultimately leading to a diminished immature neutrophil progenitor pool.

16
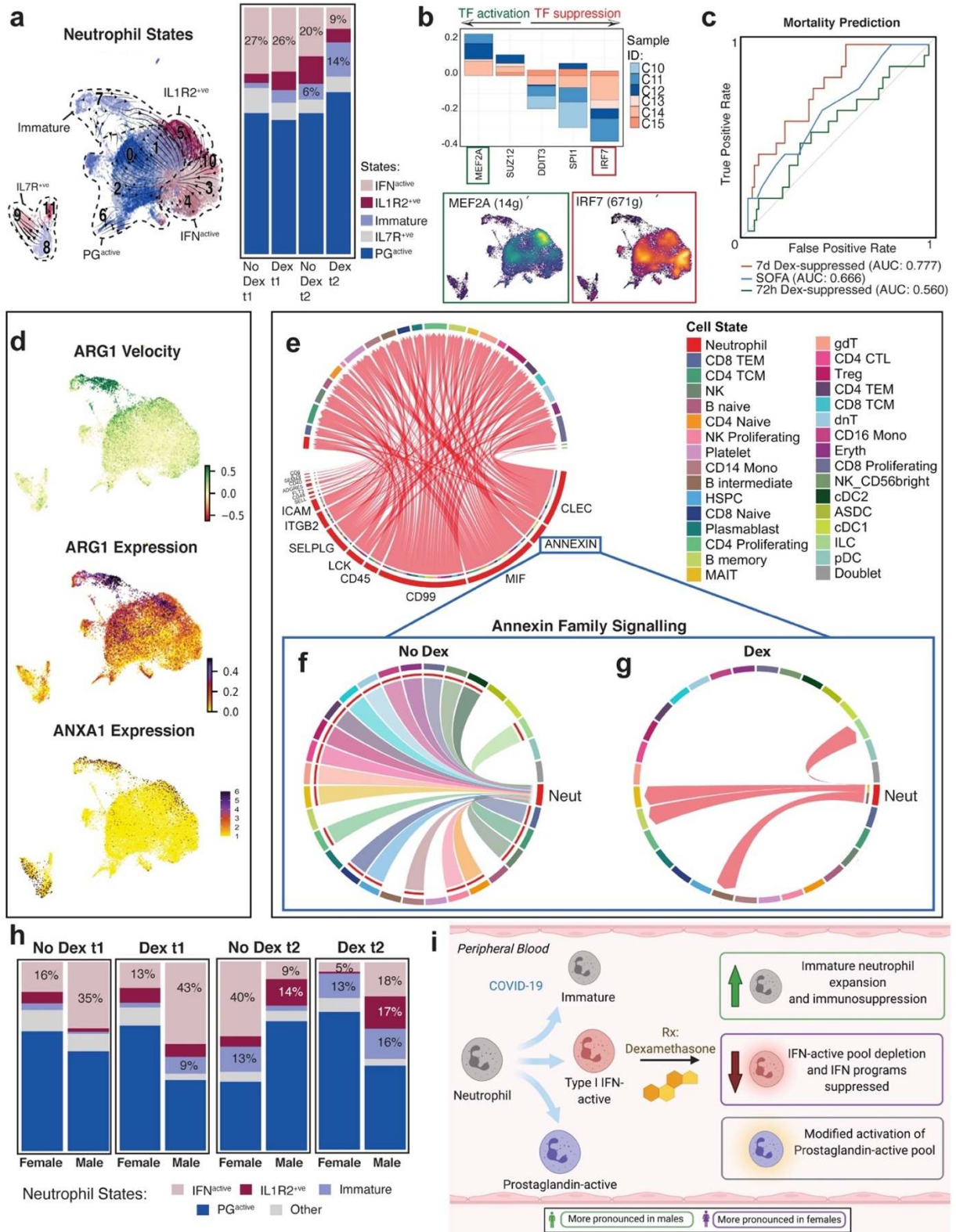
Figure 4 – Dexamethasone expands immunosuppressive neutrophils and their interactions in COVID-19. a. Neutrophil states mapped onto Louvain-clustered UMAP, with comparison of neutrophil composition between dexamethasone- and non-dexamethasone-treated samples at t1 and t2. **b.** Consensus

311   TFs activated or suppressed post-dexamethasone in at least 3 of 6 patients at t1 and predicted activity of
312   MEF2A and IRF7, two of the most differentially regulated TFs post-dexamethasone. **c.** Receiver
313   operating characteristic (ROC) curves assessing the discriminatory capacity of dexamethasone suppressed
314   DEGs at t1, t2, and sequential organ failure assessment (SOFA) scores for predicting 28-day mortality in
315   a validation cohort of 103 bulk whole blood RNA-Seq samples where 17 cases were fatal. **d.** Immature
316   and IL1R2^{+ve} neutrophil subsets express high levels of immunosuppressive neutrophil marker ARG1 and
317   ANXA1. **e.** Neutrophil-driven signaling pathways induced post-dexamethasone, identified using CellChat
318   (MHC-I signalling filtered out). **f, g**. Topology of annexin signalling without (e) and with dexamethasone
319   (f) treatment (edges filtered to those where neutrophils function as senders or recipients of annexin
320   signals). **h.** Neutrophil state composition separated by sex and dexamethasone status at t1 and t2. **i.**
321   Schematic summarizing the effects of dexamethasone on neutrophil fates and function in COVID-19
322   following dexamethasone treatment.

323

324   **Conclusions**

325   Surviving SARS-CoV-2 infection depends on striking a temporal balance between inciting viral clearance

326   immune programs during the early stage and subsequently restraining those same programs at later stages

327   to limit immunity-induced tissue damage. IFN signaling stands at the nexus between antiviral immunity

328   and over active effector immune programs that inadvertently compromise tissue function and threaten

329   survival[43]. Our work uncovered downstream IFN signalling as a signature of a stable neutrophil state that

330   is selectively expanded during late stage COVID-19 infection from a common pool of immature

331   progenitors. Given that inborn errors [25] and suppressed *early stage* [6] IFN signalling predicts COVID-19

332   severity, increased IFN^{active} neutrophils in females correlated with decreased mortality[44], and early

333   initiation of IFN therapy has been suggested to mitigate disease severity [45,46], one may posit that IFN

334   activity in neutrophils represents a concerted host antiviral program.

335   Interestingly, immunosuppression with dexamethasone, a corticosteroid known to improve mortality in

336   hospitalized COVID-19 patients[27], was associated with suppressed COVID19-specific IFN regulatory

337   networks and depleted COVID19-enriched IFN^{active} neutrophils in favour of expanding immature (ARG1^{+}

338   immunosuppressive) neutrophils. These altered neutrophil states shared striking resemblances to bacterial

339   ARDS, suggesting installation of generalized microbicidal programs ameliorate the overzealous

340   neutrophil responses during COVID-19 (and perhaps during other viral infections). While neutrophil ISG

341   activation may promote anti-viral immunity during early stages of SARS-CoV-2 infection, sustained IFN

18

342   activation during *late stages* (e.g., critically ill patients requiring intensive care) could drive

343   immunopathology of COVID-19. Indeed, positive correlation between neutrophil Type 1 IFN programs

344   and COVID-19 severity[7,47] paired with our observation that IFN[active] neutrophils dominate the

345   bronchoalveolar microenvironment during severe COVID-19 [11]directly support this view.

346   Immunotherapies that support the innate antiviral immune response by decoupling IFN-exaggerated

347   neutrophil response whilst reinforcing acquisition of suppressor states may limit the pathogenic potential

348   of neutrophils and provide tremendous clinical benefit for treating severe COVID-19.

349   There are three major limitations of our study. First, non-random group allocation (since the timing of the

350   RECOVERY trial made dexamethasone standard of care overnight) and small sample size may

351   inadvertently introduce selection bias and limit generalizability of dexamethasone findings. Second,

352   comparisons were against bacterial ARDS, and not related respiratory viral infections (i.e., H1N1

353   influenza) since public health measures eradicated such cases; this precludes assessment of whether the

354   dynamics defined are specific to SARS-CoV-2. Finally, a subset of patients sampled at t1 were

355   discharged from ICU prior to t2 collection (non-random or non-ignorable missing data), precluding

356   unbiased estimation of temporal changes between timepoints.

357   **Methods**

358   **Patient enrolment.** All patients were enrolled following admission to any of the four adult intensive care

359   units at South Health Campus, Rockyview General Hospital, Foothills Medical Center or Peter Lougheed

360   Center in Calgary, Alberta, Canada (Extended Fig 1). Patient admission to the ICU was determined by the

361   attending ICU physician based on the need for life sustaining interventions, monitoring and life-support.

362   The research teams did not participate in clinical decisions. Study inclusion required a minimal age of 18,

363   the ability to provide consent, or for most participants, the ability of a surrogate decision maker to provide

364   regained capacity consent. All participants required an arterial catheter for blood draws, but the insertion

365   of this catheter was at the discretion of the attending medical team. Participants required a positive

366   clinical RNA COVID-19 test prior to enrolment, and evidence of bilateral lung infiltrates and hypoxemia

367   consistent with ARDS. At the time of sample collections, all COVID-19$^+$ enrolled individuals were

368   culture negative for concurrent bacterial infections in the blood, urine, and sputum. The bacterial ARDS

369   cohort required a negative COVID-19 test and a definitive microbiological diagnosis of bacterial

370   pneumonia with chest imaging consistent with a diagnosis of ARDS. Patients were excluded from our

371   study if they: 1. were on immunosuppressive therapies, 2. had established autoimmune disease, or 3. had

372   active malignancy. Since tocilizumab or other immunomodulatory agents were not approved for use in

373   patients with severe COVID-19 in Alberta over the timespan of this study, none of them received these

374   medications. While bacterial sepsis patients received appropriate antibiotic treatments, none were

375   prescribed immunosuppressive or steroid therapy. All bacterial sepsis patients had lung infections caused

376   by gram-positive cocci (4 *Staphylococcus aureus* and 2 *Streptococcus pneumoniae*). Participants were

377   required to have a definitive diagnosis and appropriate consent and samples collected within 72hrs of

378   admission to the ICU in order to be included. Timepoint 1 (T1) refers to the first blood draw, while T2

379   was a repeat blood draw taken 7 days after T1, if the participant remained in the ICU, and had an arterial

380   catheter. For each participant, whole blood was collected via the arterial catheter and immediately

381   processed for analysis. Healthy blood donors were recruited by university-wide advertisement and

382   required that participants were: 1. not on immunomodulatory medications, 2. were asymptomatic for

383   SARS-CoV-2, 3. did not receive vaccination against SARS-CoV-2, and 4. did not have underlying

384   immune disorders.

385   **Epidemiological analysis.** We used the Alberta provincial eCRITICAL oracle-based analytics database

386   (Tracer) to query and extract Alberta COVID-19 ICU cases and volumes for this study[48]. Aggregate data

387   from sixteen individual adult ICUs was obtained over the study periods. The administration of

388   dexamethasone was not possible to capture at an aggregate level; therefore, we queried the database for

389   patients admitted to ICU prior to dexamethasone becoming standard of care in our Province (pre-

390   dexamethasone era; January 2020 till May 31st, 2020) versus dexamethasone as standard of care for

391   severe COVID-19 (June 1st, 2020, till May 31st, 2021). Tocilizumab was approved for use in Alberta

20

392   March 11 2021, and a small supply (150 doses) was obtained for severe COVID-19 patients after this

393   date.

394   **Human Study Ethics**. All work with humans was approved by the Conjoint Health Research Ethics

395   Board (CHREB) at the University of Calgary (Ethics ID: REB20-0481) and is consistent with the

396   Declaration of Helsinki.

397   **Serum cytokine assessment.** Cytokines, chemokines and soluble cytokine receptors were quantitated on

398   multiplex arrays that included a 65 MIlliPLEX cytokine/chemokine (6Ckine, BCA-1, CTACK, EGF,

399   ENA-78, Eotaxin, Eotaxin-2, Eotaxin-3, FGF-2, Flt-3L, Fractalkine, G-CSF, GM-CSF, GRO, I-309,

400   IFNα2, IFNγ, IL-1α, IL-1β, IL-1ra, IL-2, IL-3, IL-4, IL-5, IL-6, IL-7, IL-8, IL-9, IL-10, IL-12 (p40), IL-

401   12 (p70), IL-13, IL-15, IL-16, IL-17A, IL-18, IL-20, IL-21, IL-23, IL-28a, IL-33, IP-10, LIF, MCP-1,

402   MCP-2, MCP-3, MCP-4, MDC, MIP-1α, MIP-1β, MIP-1d, PDGF-AA, PDGF-AB/BB, RANTES, SDF-1

403   a+b, sCD40L, SCF,TARC, TGFa, TNFa, TNFb, TPO, TRAIL, TSLP, VEGF) and a 14 MilliPLEX

404   soluble cytokine (sCD30, sEGFR, sgp130, sIL-1RI, sIL-1RII, sIL-2Ra, sIL-4R, sIL-6R, sRAGE, sTNF

405   RI, sTNF RII, sVEGF R1, sVEGF R2, sVEGF R3) arrays (Millipore Sigma, Oakville, ON, Canada) on a

406   Luminex Model 200 Luminometer (Luminex Corporation, Austin, TX). EDTA-plasma samples were

407   collected from each patient by venipuncture following a standard operating protocol (SOP) and stored at -

408   80C until tested. Each run included a full range of calibrators. The Mann-Whitney U test was used to

409   compare groups and p-values were adjusted for multiple comparisons using Holm-Šídák stepdown

410   method with alpha set to 0.05.

411   **Shotgun proteomics using Liquid Chromatography and Mass Spectrometry (LC-MS/MS)**

412   The serum of COVID-19 patients (COVID-19 = 9, dexamethasone-treated = 4) and bacterial ARDS

413   controls (N = 6) were collected and subjected to quantitative proteomics. The total protein concentrations

414   were determined by Pierce™ BCA Protein Assay Kit (23225, ThermoFisher). A trichloroacetic acid

415   (TCA)/acetone protocol was used to pellet 100μg of proteins per sample. Samples were subjected to a

21

416   quantitative proteomics workflow as per supplier (Thermo Fisher) recommendations. Samples were

417   reduced in 200mM tris(2-carboxyethyl)phosphine (TCEP), for 1h at 55°C, reduced cysteines were

418   alkylated by incubation with iodoacetamide solution (50mM) for 20min at room temperature. Samples

419   were precipitated by acetone/methanol, and 600μL ice-cold acetone was added followed by incubation at

420   -20°C overnight. A protein pellet was obtained by centrifugation ($8,000g$, 10min, 4°C) followed by

421   acetone drying (2min). Precipitated pellet was resuspended in100 μL of 50mM triethylammonium

422   bicarbonate (TEAB) buffer followed by tryptase digestion (5μg trypsin per 100μg of protein) overnight at

423   37°C. TMT-6plex™ Isobaric Labeling Reagents (90061, Thermo Fisher) were resuspended in anhydrous

424   acetonitrile and added to each sample (41μL TMT-6plex™ per 100μL sample) and incubated at room

425   temperature for 1h. The TMT labeling reaction was quenched by 2.5% hydroxylamine for 15min at room

426   temperature. TMT labeled samples were combined and acidified in 100% trifluoroacetic acid to pH < 3.0

427   and subjected to C18 chromatography (Sep-Pak) according to manufacturer recommendations. Samples

428   were stored at -80°C before lyophilization, followed by resuspension in 1% formic acid before liquid

429   chromatography and tandem mass spectrometry analysis.

430   Tryptic peptides were analyzed on an Orbitrap Fusion Lumos Tribrid mass spectrometer (Thermo

431   Scientific) operated with Xcalibur (version 4.0.21.10) and coupled to a Thermo Scientific Easy-nLC

432   (nanoflow liquid chromatography) 1200 System. Tryptic peptides (2μg) were loaded onto a C18 trap

433   (75μm x 2cm; Acclaim PepMap 100, P/N 164946; ThermoFisher) at a flow rate of 2μL/min of solvent A

434   (0.1% formic acid in LC-MS grade H2O). Peptides were eluted using a 120min gradient from 5 to 40%

435   (5% to 28% in 105min followed by an increase to 40% B in 15min) of solvent B (0.1% formic acid in

436   80% LC-MS grade acetonitrile) at a flow rate of 0.3μL/min and separated on a C18 analytical column

437   (75μm x 50cm; PepMap RSLC C18; P/N ES803A; ThermoScientific). Peptides were then electrosprayed

438   using 2.1kV voltage into the ion transfer tube (300°C) of the Orbitrap Lumos operating in positive mode.

439   For LC-MS/MS measurements with the FAIMS Pro (Thermo Fisher Scientific), multiple compensation

440   voltages (CV) were applied, -40V, -60V, and -80V with a cycle time of 1 second. FAIMS was used to

441   generate technical replicates from plex 1 to 6. The Orbitrap first performed a full MS scan at a resolution

442   of 120,000 FWHM to detect the precursor ion having a m/z between 375 and 1,575 and a +2 to +4 charge.

443   The Orbitrap AGC (Auto Gain Control) and the maximum injection time were set at 4×10^5 and 50ms,

444   respectively. The Orbitrap was operated using the top speed mode with a 3 second cycle time for

445   precursor selection. The most intense precursor ions presenting a peptidic isotopic profile and having an

446   intensity threshold of at least 2×10^4 were isolated using the quadrupole (Isolation window (m/z) of 0.7)

447   and fragmented using HCD (38% collision energy) in the ion routing multipole. The fragment ions (MS2)

448   were analyzed in the Orbitrap at a resolution of 15,000. The AGC and the maximum injection time were

449   set at 1×10^5 and 105ms, respectively. The first mass for the MS2 was set at 100 to acquire the TMT

450   reporter ions. Dynamic exclusion was enabled for 45 seconds to avoid of the acquisition of same

451   precursor ion having a similar m/z (plus or minus 10ppm).

452   **Proteomic data and bioinformatics analysis**

453   Spectral data acquired from the mass spectrometer were matched to peptide sequences using MaxQuant

454   software (v.1.6.14)[49]. Due to a lack of direct compatibility with Maxquant, spectra generated using the

455   FAIMS pro was first converted to MzXML using the FAIMS MzXML Generator from the Coon's lab

456   (https://github.com/coongroup/FAIMS-MzXML-Generator). Next, peptide sequences from the human

457   proteome and Sars-CoV-2 proteins were obtained from the UniProt database (May 2021) and matched

458   using the Andromeda[50] algorithm at a peptide-spectrum match false discovery rate (FDR) of 0.05. Search

459   parameters included a mass tolerance of 20 p.p.m. for the parent ion, 0.5 Da for the fragment ion,

460   carbamidomethylation of cysteine residues (+57.021464 Da), variable N-terminal modification by

461   acetylation (+42.010565 Da), and variable methionine oxidation (+15.994915 Da). Relative quantification

462   was set as TMT 6-plex labels 126 to 131. The cleavage site specificity was set to Trypsin/P, with up to

463   two missed cleavages allowed. Next, the evidence.txt and proteinGroups.txt were loaded into the R

464   software (v4.0.2) for statistical analysis. The normalization and identification of differentially expressed

465   proteins was performed using the MSstatsTMT package[51]. Multiple comparisons were corrected using the

466   Benjamini-Hochberg approach.

467   **Leukocyte and lymphocyte isolation.** For lymphocyte isolation, whole blood (2mL) was collected in

468   5mL polystyrene round-bottom heparinized vacutubes. To isolate lymphocytes by immunomagnetic

469   negative selection, 100μL of Isolation Cocktail and 100μL of Rapid Spheres (EasySep™ Direct Human

470   Total Lymphocytes Isolation Kit: 19655, StemCell Technologies) were added to 2 mL of whole blood.

471   After mixing and 5min incubation at RT, the sample volumes were topped up to 2.5mL with 0.04%

472   bovine serum albumin (BSA) in PBS. The diluted sample was incubated in the magnet without lid for

473   5min, at RT and negatively selected lymphocytes were decanted into a new 5 mL polystyrene tube.

474   Except the addition of Isolation Cocktail, all steps were repeated once. The final lymphocyte cell

475   suspension was transferred to a 15 mL polypropylene tube and a volume of 5mL 0.04% BSA in PBS was

476   added to the sample. Lymphocytes were precipitated by centrifugation for 5 min at 2000rpm, supernatant

477   was discarded, and cells were resuspended in 5 mL of 0.04% BSA in PBS. This last step was repeated

478   once, and cells were then resuspended in 100 μL of PBS+0.04% BSA. Cell density was quantified with a

479   hemacytometer, cell viability was assessed with Trypan Blue staining (T8154; Sigma Aldrich), and 7500

480   live lymphocytes were transferred to a sterile 1.5 mL microcentrifuge tube.

481   For leukocyte isolation, 1 mL of whole blood from heparin containing vacutubes was transferred to 5 mL

482   polystyrene round-bottom tubes and 12μL of 0.5M EDTA was added. 2% FBS in PBS (1mL) and 50μL

483   of EasySep RBC Depletion spheres (EasySep™ RBC Depletion Reagent: 18170, Stem Cell

484   Technologies) were added to immunomagnetically deplete red blood cells. After 5 min of magnet

485   incubation at RT, cell suspension containing leukocytes was decanted into a new 5mL polystyrene tube.

486   To ensure complete removal of red blood cells, RBC depletion was repeated, and cell suspension

487   containing leukocytes was decanted into a new 15mL polypropylene tube. Leukocytes were precipitated

488   by centrifugation at 2000rpm for 5 min at 20ºC and resuspended in 5mL of 0.04% BSA in PBS. This last

489   step was repeated once, and leukocytes were resuspended in 2 mL of 0.04% BSA in PBS. Cell viability

24

490 and cell density were assessed, and 7500 live leukocytes were transferred to the microcentrifuge tube

491 containing the lymphocyte cell suspension. The volume of the cell suspension containing 7500

492 lymphocytes and 7500 leukocytes in a total of 50 µL of 0.04% BSA in PBS.

493 **Immunocytochemistry and immunohistochemistry**

494 Isolated leukocyte and lymphocyte samples were fixed in 4% paraformaldahyde in PBS (0.2mM and

495 pH7.4), and spun in a cytocentrifuge (8min at 300g) onto coated slides. Pathological lung sections (FFPE

496 fixed and sectioned at 5um) were deparaffinized in Slide Brite (Fisher Scientific NC968653) and

497 rehydrated. Slides were permeabilized and blocked with 10% normal donkey serum in PBS (with 0.5%

498 triton X-100), primary antibodies (S100A8/9 Abcam ab22506; IFITM1 Abcam ab233545) were

499 incubated at 4°C overnight, followed by incubation with donkey anti-rabbit-Alexa488 (Invitrogen

500 A32790) or anti-mouse-Alexa555 (Invitrogen A31570) for 1h at room temperature (RT). Cytospun slides

501 were sequentially stained with CD24 (Abcam ab202073) on the same slides for 1h at RT, followed by

502 donkey anti-rabbit-Alexa647 (Invitrogen A31573). Imaging was done using a VS-120 slide scanner

503 (Olympus) and high resolution image imaging was done using an SP8 spectral confocal microscope

504 (Leica). Image processing was completed in Fiji [52].

505 **Single-cell RNA-Seq library construction, alignment, and quality control.** A total of 15,000 single

506 cells (containing an equal proportion of leukocytes and lymphocytes) were loaded for partitioning using

507 10X Genomics NextGEM Gel Bead emulsions (Version 3.1). All samples were processed as per

508 manufacturer's protocol (with both PCR amplification steps run 12X). Quality control of resulting

509 libararies and quantification was performed using TapeStation D1000 ScreenTape assay (Agilent).

510 Sequencing was performed using Illumina NovaSeq S2 and SP 100 cycle dual lane flow cells over

511 multiple rounds to ensure each sample received approximately 32,000 reads per cell. Sequencing reads

512 were aligned using CellRanger 3.1.0 pipeline[53] to the standard pre-built GRCh38 reference genome.

513 Samples that passed alignment QC were aggregated into single datasets using CellRanger aggr with

514 between-sample normalization to ensure each sample received an equal number of mapped reads per cell.

515   Aggregated non-dexamethasone-treated COVID-19 (n = 12) and bacterial ARDS (n = 9) samples

516   recovered 1,872,659 cells that were sequenced to 38,410 post-normalization reads per cell. Likewise,

517   aggregated COVID-19 samples with (n = 9) or without (n = 12) dexamethasone recovered 1,748,551

518   single cells sequenced to 51,415 post-normalization reads per cell. Aggregated healthy samples recovered

519   19,816 cells, including 1,912 post-QC neutrophils (n = 5).

520   **Single-cell RNA-Seq computational analyses and workflows.** Filtered feature-barcode HDF5 matrices

521   from aggregated datasets were imported into the R package Seurat v.3.9 for normalization, scaling,

522   integration, multi-modal reference mapping, louvain clustering, dimensionality reduction, differential

523   expression analysis, and visualization [54]. Briefly, cells with abnormal transcriptional complexity (fewer

524   than 500 UMIs, greater than 25,000 UMIs, or greater than 25% of mitochondrial reads) were considered

525   artifacts and were removed from subsequent analysis. Since granulocytes have relatively low RNA

526   content (due to high levels of RNases), QC thresholds were informed by [8] as they recently defined several

527   rodent and human neutrophil subsets from scRNA-Seq samples. Cell identity was classified by mapping

528   single cell profiles to the recently published PBMC single-cell joint RNA/CITE-Seq multi-omic reference

529   [55].

530   **Annotation of neutrophil states.** Since no published reference automates granulocyte annotations,

531   neutrophil clusters were manually annotated by querying known markers (i.e. CSF3R, S100A8, S100A9,

532   MMP8, MMP9, ELANE, MPO)[56] and were corroborated using the R package SingleR[57]. Neutrophil

533   states were defined by grouping unsupervised (louvain at default resolution) subclusters based on two

534   overlapping criteria: scVelo-inferred neutrophil maturity, and 2. by corroborating gene expression and

535   SCENIC-inferred GRN signatures with previous human and rodent neutrophil scRNA-Seq studies.

536   Immature neutrophils were defined as $CD24^+ARG1^+ELANE^+MPO^+ATF4^{GRN-active}JDP2^{GRN-active}$

537   neutrophils [7,8,47,58] that were reproducibly assigned as 'root cells' in scVelo-based latent time pseudo-

538   ordering. IFN^{active} neutrophils were defined by preferential mRNA splicing (positive velocity) and

539   expression of IFN-stimulated genes such as IFITM1/2, IFIT1/2/3, ISG15/20, and IFI6/27/44/44L [6,44,59].

26

540   PG^{active} neutrophils were distinguished by preferential splicing of PTGS2/COX2 (as well as expression for

541   prostaglandin transport LST1) [44] and included a subset that expressed high levels of IL1β decoy receptor

542   IL1R2 [33]. Lastly, IL7R$^+$ neutrophils (a small but distinct subset that maybe of thymic origin [60] expressed

543   high levels of ribosomal subunit genes (e.g. RPL5/7A/8/13/18/19/23/24/27/P0) that are highly

544   reminiscent of 'ribosomal^{hi}-specific cluster 7' identified previously [47].

545   **Statistical approach for comparing cell proportions.** To test whether cell composition was changed

546   due to infection type (COVID-19 versus Bacterial ARDS) or treatment group (dexamethasone versus

547   non-dexamethasone), a generalized linear mixed-effects model was employed where infection type and

548   treatment group were considered fixed and individual patients were considered random effect. Fitting was

549   done with Laplace approximation using the 'glmer' function in the 'lme4' R package [61] and p-values were

550   calculated using the R package 'car'. Boxplots comparing cell type composition were generated using the

551   ggplot2 package. Since a subset of patients sampled at t1 were discharged from ICU prior to t2 collection

552   (non-random or non-ignorable missing data), we limit statistical comparisons to between group

553   comparisons within one time point (e.g., COVID-19 72h vs Bacterial ARDS 72hr, dexamethasone-treated

554   72h vs non-dexamethasone-treated 72h) and do not estimate temporal differences across t1 and t2.

555   **Inferring cell communication networks.** Differential cell-cell interaction networks were reconstructed

556   using the Connectome R toolkit v0.2.2[62] and CellChat v1.0.0 [63]. Briefly, *DifferentialConnectome* queried

557   Seurat R objects housing datasets integrated by infection type and dexamethasone status to define nodes

558   and edges for downstream network analysis. Total number of interactions and interaction strengths were

559   calculated using CellChat's *compareInteractions* function. Differential edge list was passed through

560   *CircosDiff* (a wrapper around the R package 'circlize') and CellChat's *netVisual_chord_gene* to filter

561   receptor-ligand edges and generate Circos plots.

562   **Consensus DEGs and perturbation scores**. Differentially expressed genes (DEGs) were those with an

563   average log fold change (FC) greater than 0.25 (p-adjusted < 0.05) as determined by Seurat's Wilcoxon

564   rank-sum test. Consensus stacked bars showing cumulative log fold changes (colored by individual

27

565   sample contributions) were generated using *constructConsensus* function [7] for genes exhibiting

566   reproducible changes across patients (>3 for 72-hour comparisons, > 2 for 7-day comparisons). Gene Set

567   Enrichment analyses of consensus DEGs were performed using gProfiler's g:GOSt (p-value cutoff

568   <0.05). A cell state-specific 'perturbation score' was calculated to reflect the magnitude of response

569   elicited by factoring in number and cumulative FC of consensus DEGs. Perturbation scores were

570   visualized using Nebulosa-generated density plots [64].

571   **Constructing cellular trajectories using RNA velocity.** Analysis of neutrophil trajectories was

572   performed by realigning CellRanger count-generated BAMs with RNA velocity command-line tool [20]

573   using the *run10x* command and human (GRCh38) annotations. The output loom files containing spliced

574   and unspliced counts were combined to compare neutrophils in COVID-19 with Bacterial ARDS controls

575   and dexamethasone-treated with non-treated COVID-19 patients. For both analyses, combined looms

576   were imported into Seurat v.3.9 using the *ReadVelocity* function in SeuratWrappers v.0.2.0, normalized

577   using *SCTransform* v.0.3.2 [65], reduced and projected onto a UMAP, and exported as a .h5 file using the

578   *SaveH5Seurat* function. Counts stored in H5 files were imported, filtered, and normalized as

579   recommended in the scVelo v.0.2.1 workflow [19]. RNA velocities were estimated using stochastic and

580   dynamical models. Since both models yielded comparable results, stochastic model was used as default

581   for all subsequent analyses. Calculations stored in AnnData's metadata were exported as CSVs and kernel

582   density lines depicting Velocity-inferred latent time distribution were plotted with ggplot2 v.3.1.1.

583   **Gene Regulatory Network reconstruction.** Single-cell regulatory network inference and clustering

584   (SCENIC)[26] was employed to infer regulatory interactions between transcription factors (TFs) and their

585   targetome by calculating and pruning co-expression modules. Briefly, neutrophils were subsetted from

586   scVelo-realigned Seurat object and processed using default and recommended parameters specified in

587   SCENIC's vignette (https://github.com/aertslab/SCENIC) using the hg19 RcisTarget reference. Regulon

588   activity scores (in '3.4_regulonAUC.Rds', an output of the SCENIC workflow) were added to scVelo

589   object (using *CreateAssayObject* function) to jointly project trajectory and TF activity onto the same

28

590   UMAP embeddings. Consensus stacked bars showing cumulative logFC of AUCell scores for each TF

591   (colored by individual sample contributions) were generated by modifying the *constructConsensus*

592   function[7] for SCENIC assay. Targetome of TFs predicted as drivers of neutrophil states (stored in

593   '2.6_regulons_asGeneSet.Rds') was profiled using g:Profiler's functional enrichment analysis and genes

594   intersecting with the Interferon pathway were plotted using iRegulon (Cytoscape plugin)[66].

595   **Comparing scRNA-Seq findings with published datasets.** To test whether dexamethasone-suppressed

596   neutrophil genes at t1 and t2 (Extended Data Table 4) predicted COVID-19 mortality, we repurposed

597   methods described in [33] and employed whole blood bulk RNA-Seq datasets generated by [34] as a validation

598   cohort of 103 samples (where 17 were fatal). Briefly, each of the 103 samples were scored by the

599   aggregated expression of dexamethasone-suppressed neutrophil consensus genes at t1 and t2 using

600   Seurat's AddModuleScore(). Dexamethasone-suppressed module scores were used as the predictor

601   variable and 28-day mortality was used as the response variable to construct an ROC curve using pROC's

602   roc() function. To infer bronchoalveolar neutrophil composition in severe and moderate COVID-19 [11]and

603   across bacterial pneumonia and COVID-19 [32], neutrophils ($CSF3R^+$, $S100A8^+$, $S100A9^+$) captured in

604   BALF scRNA-Seq datasets were projected onto our peripheral blood reference using mutual nearest

605   neighbor anchoring (FindTransferAnchors) and identity transferring (TransferData and AddMetaData)

606   strategy implemented in Seurat v4 [54].

607   **COVID Neutrophil Atlas.** To enable intuitive exploration of single-cell datasets, a web portal

608   (http://biernaskielab.ca/covid_neutrophil or http://biernaskielab.com/covid_neutrophil) was built using

609   RShiny v1.1.0, shinyLP v.1.1.2, and shinythemes v.1.1.2 packages.

610   **Data availability.** Single cell RNA-Seq datasets are available at NCBI GEO (which automatically makes

611   SRA deposit) at the following accession: GSE157789. Single-cell datasets can be further explored on our

612   companion portal at http://biernaskielab.ca/COVID_neutrophil or

613   http://biernaskielab.com/COVID_neutrophil. Velocyto-generated LOOM files and processed R objects

614   are available for reanalysis from: http://doi.org/10.6084/m9.figshare.14330795. Whole blood bulk RNA-

615   Seq datasets employed as an independent validation cohort were downloaded from GSE157103. BALF

616   scRNA-Seq datasets from severe and moderate COVID-19 were downloaded from GSE145926.

617   Processed BALF scRNA-Seq objects from patients with bacterial pneumonia and COVID-19 (archived at

618   GSE167118) were downloaded from authors' archive: https://figshare.com/articles/dataset/_/13608734.

619   Mass spectrometry datasets will be available via PRIDE Archive (http://www.ebi.ac.uk/pride/archive), it

620   has been submitted (submission #: 1-20210702-114055) and is pending accessioning.

621   Proteomics data will be available at PRIDE (https://www.ebi.ac.uk/pride/), it has been submitted

622   (submission #: 1-20210702-114055) and is pending accessioning.

623   **Code availability.** All analyses were performed using publicly available software as described in the

624   methods section. Raw scripts are available upon request.

625   **Supplementary Information** is available for this paper.

30

References:

648

649 1   Matthay, M. A. *et al.* Acute respiratory distress syndrome. *Nat Rev Dis Primers* **5**, 18,
650   doi:10.1038/s41572-019-0069-0 (2019).
651 2   Wang, D. *et al.* Clinical Characteristics of 138 Hospitalized Patients With 2019 Novel
652   Coronavirus–Infected Pneumonia in Wuhan, China. *JAMA* **323**, 1061-1069,
653   doi:10.1001/jama.2020.1585 (2020).
654 3   Zhu, N. *et al.* A Novel Coronavirus from Patients with Pneumonia in China, 2019. *N Engl J Med*
655   **382**, 727-733, doi:10.1056/NEJMoa2001017 (2020).
656 4   Middleton, E. A. *et al.* Neutrophil extracellular traps contribute to immunothrombosis in COVID-
657   19 acute respiratory distress syndrome. *Blood* **136**, 1169-1179, doi:10.1182/blood.2020007008
658   (2020).
659 5   Veras, F. P. *et al.* SARS-CoV-2-triggered neutrophil extracellular traps mediate COVID-19
660   pathology. *J Exp Med* **217**, doi:10.1084/jem.20201129 (2020).
661 6   Combes, A. J. *et al.* Global absence and targeting of protective immune states in severe COVID-
662   19. *Nature*, doi:10.1038/s41586-021-03234-7 (2021).
663 7   Wilk, A. J. *et al.* A single-cell atlas of the peripheral immune response in patients with severe
664   COVID-19. *Nat Med* **26**, 1070-1076, doi:10.1038/s41591-020-0944-y (2020).
665 8   Xie, X. *et al.* Single-cell transcriptome profiling reveals neutrophil heterogeneity in homeostasis
666   and infection. *Nature Immunology* **21**, 1119-1133, doi:10.1038/s41590-020-0736-z (2020).
667 9   Lee, J. S. *et al.* Immunophenotyping of COVID-19 and influenza highlights the role of type I
668   interferons in development of severe COVID-19. *Science Immunology* **5**, eabd1554,
669   doi:10.1126/sciimmunol.abd1554 (2020).
670 10 Xu, G. *et al.* The differential immune responses to COVID-19 in peripheral and lung revealed by
671   single-cell RNA sequencing. *Cell Discovery* **6**, 73, doi:10.1038/s41421-020-00225-2 (2020).
672 11 Liao, M. *et al.* Single-cell landscape of bronchoalveolar immune cells in patients with COVID-19.
673   *Nature Medicine* **26**, 842-844, doi:10.1038/s41591-020-0901-9 (2020).
674 12 Wauters, E. *et al.* Discriminating mild from critical COVID-19 by innate and adaptive immune
675   single-cell profiling of bronchoalveolar lavages. *Cell Research* **31**, 272-290, doi:10.1038/s41422-
676   020-00455-9 (2021).
677 13 Rosin, N. L. *et al.* SARS-CoV-2 infection of circulating immune cells is not responsible for virus
678   dissemination in severe COVID-19 patients. *bioRxiv*, 2021.2001.2019.427282,
679   doi:10.1101/2021.01.19.427282 (2021).
680 14 Ranieri, V. M. *et al.* Acute respiratory distress syndrome: the Berlin Definition. *JAMA* **307**, 2526-
681   2533, doi:10.1001/jama.2012.5669 (2012).
682 15 Mehta, P. *et al.* COVID-19: consider cytokine storm syndromes and immunosuppression. *Lancet*
683   **395**, 1033-1034, doi:10.1016/s0140-6736(20)30628-0 (2020).
684 16 Feng, Z. *et al.* Early prediction of disease progression in COVID-19 pneumonia patients with
685   chest CT and clinical characteristics. *Nat Commun* **11**, 4968, doi:10.1038/s41467-020-18786-x
686   (2020).
687 17 Wu, C. *et al.* Risk Factors Associated With Acute Respiratory Distress Syndrome and Death in
688   Patients With Coronavirus Disease 2019 Pneumonia in Wuhan, China. *JAMA Intern Med*,
689   doi:10.1001/jamainternmed.2020.0994 (2020).
690 18 Barnes, B. J. *et al.* Targeting potential drivers of COVID-19: Neutrophil extracellular traps. *J Exp
691   Med* **217**, doi:10.1084/jem.20200652 (2020).
692 19 Bergen, V., Lange, M., Peidli, S., Wolf, F. A. & Theis, F. J. Generalizing RNA velocity to transient
693   cell states through dynamical modeling. *Nature Biotechnology* **38**, 1408-1414,
694   doi:10.1038/s41587-020-0591-3 (2020).

695   20   La Manno, G. *et al.* RNA velocity of single cells. *Nature* **560**, 494-498, doi:10.1038/s41586-018-
696   0414-6 (2018).
697   21   Chen, J. S. *et al.* Non-steroidal anti-inflammatory drugs dampen the cytokine and antibody
698   response to SARS-CoV-2 infection. *Journal of Virology*, JVI.00014-00021, doi:10.1128/JVI.00014-
699   21 (2021).
700   22   Takashima, A. & Yao, Y. Neutrophil plasticity: acquisition of phenotype and functionality of
701   antigen-presenting cell. *J Leukoc Biol*, doi:10.1189/jlb.1MR1014-502R (2015).
702   23   Ledford, J. G., Kovarova, M. & Koller, B. H. Impaired Host Defense in Mice Lacking ONZIN. *The
703   Journal of Immunology* **178**, 5132, doi:10.4049/jimmunol.178.8.5132 (2007).
704   24   Zhang, Q. *et al.* in *Med (N Y)* Vol. 1   14-20 (© 2020 Elsevier Inc., 2020).
705   25   Zhang, Q. *et al.* Inborn errors of type I IFN immunity in patients with life-threatening COVID-19.
706   *Science* **370**, doi:10.1126/science.abd4570 (2020).
707   26   Aibar, S. *et al.* SCENIC: single-cell regulatory network inference and clustering. *Nat Methods* **14**,
708   1083-1086, doi:10.1038/nmeth.4463 (2017).
709   27   Horby, P. *et al.* Dexamethasone in Hospitalized Patients with Covid-19 - Preliminary Report. *N
710   Engl J Med*, doi:10.1056/NEJMoa2021436 (2020).
711   28   Mahler, M., Meroni, P. L., Infantino, M., Buhler, K. A. & Fritzler, M. J. Circulating Calprotectin as a
712   Biomarker of COVID-19 Severity. *Expert Rev Clin Immunol* **17**, 431-443,
713   doi:10.1080/1744666X.2021.1905526 (2021).
714   29   Demichev, V. *et al.* A time-resolved proteomic and prognostic map of COVID-19. *Cell Syst*,
715   doi:10.1016/j.cels.2021.05.005 (2021).
716   30   Park, J. *et al.* In-depth blood proteome profiling analysis revealed distinct functional
717   characteristics of plasma proteins between severe and non-severe COVID-19 patients. *Sci Rep*
718   **10**, 22418, doi:10.1038/s41598-020-80120-8 (2020).
719   31   Shu, T. *et al.* Plasma Proteomics Identify Biomarkers and Pathogenesis of COVID-19. *Immunity*
720   **53**, 1108-1122 e1105, doi:10.1016/j.immuni.2020.10.008 (2020).
721   32   Zhao, Y. *et al.* Clonal expansion and activation of tissue-resident memory-like T$_H$17
722   cells expressing GM-CSF in the lungs of patients with severe COVID-19. *Science Immunology* **6**,
723   eabf6692, doi:10.1126/sciimmunol.abf6692 (2021).
724   33   Wilk, A. J. *et al.* Multi-omic profiling reveals widespread dysregulation of innate immunity and
725   hematopoiesis in COVID-19. *Journal of Experimental Medicine* **218**, doi:10.1084/jem.20210582
726   (2021).
727   34   Overmyer, K. A. *et al.* Large-Scale Multi-omic Analysis of COVID-19 Severity. *Cell Systems* **12**, 23-
728   40.e27, doi:https://doi.org/10.1016/j.cels.2020.10.003 (2021).
729   35   Vago, J. P. *et al.* Annexin A1 modulates natural and glucocorticoid-induced resolution of
730   inflammation by enhancing neutrophil apoptosis. *Journal of Leukocyte Biology* **92**, 249-258,
731   doi:https://doi.org/10.1189/jlb.0112008 (2012).
732   36   Oliveira, L. G. *et al.* Annexin A1 Is Involved in the Resolution of Inflammatory Responses during
733   *Leishmania braziliensis* Infection. *The Journal of Immunology* **198**, 3227,
734   doi:10.4049/jimmunol.1602028 (2017).
735   37   Uhel, F. *et al.* Early Expansion of Circulating Granulocytic Myeloid-derived Suppressor Cells
736   Predicts Development of Nosocomial Infections in Patients with Sepsis. *Am J Respir Crit Care
737   Med* **196**, 315-327, doi:10.1164/rccm.201606-1143OC (2017).
738   38   Arlauckas, S. P. *et al.* Arg1 expression defines immunosuppressive subsets of tumor-associated
739   macrophages. *Theranostics* **8**, 5842-5854, doi:10.7150/thno.26888 (2018).
740   39   Derakhshani, A. *et al.* Arginase 1 (Arg1) as an Up-Regulated Gene in COVID-19 Patients: A
741   Promising Marker in COVID-19 Immunopathy. *J Clin Med* **10**, doi:10.3390/jcm10051051 (2021).

33

742 40 Kelly-Scumpia, K. M. *et al.* ER Stress Regulates Immunosuppressive Function of Myeloid Derived
743   Suppressor Cells in Leprosy that Can Be Overcome in the Presence of IFN-γ. *iScience* **23**, 101050,
744   doi:https://doi.org/10.1016/j.isci.2020.101050 (2020).
745 41 Okun, J. G. *et al.* Molecular regulation of urea cycle function by the liver glucocorticoid receptor.
746   *Mol Metab* **4**, 732-740, doi:10.1016/j.molmet.2015.07.006 (2015).
747 42 Peckham, H. *et al.* Male sex identified by global COVID-19 meta-analysis as a risk factor for death
748   and ITU admission. *Nature Communications* **11**, 6317, doi:10.1038/s41467-020-19741-6 (2020).
749 43 Park, A. & Iwasaki, A. Type I and Type III Interferons - Induction, Signaling, Evasion, and
750   Application to Combat COVID-19. *Cell host & microbe* **27**, 870-878,
751   doi:10.1016/j.chom.2020.05.008 (2020).
752 44 Gupta, S. *et al.* Sex differences in neutrophil biology modulate response to type I interferons and
753   immunometabolism. *Proceedings of the National Academy of Sciences* **117**, 16481,
754   doi:10.1073/pnas.2003603117 (2020).
755 45 Monk, P. D. *et al.* Safety and efficacy of inhaled nebulised interferon beta-1a (SNG001) for
756   treatment of SARS-CoV-2 infection: a randomised, double-blind, placebo-controlled, phase 2
757   trial. *The Lancet Respiratory Medicine* **9**, 196-206, doi:10.1016/S2213-2600(20)30511-7 (2021).
758 46 Wang, N. *et al.* Retrospective Multicenter Cohort Study Shows Early Interferon Therapy Is
759   Associated with Favorable Clinical Responses in COVID-19 Patients. *Cell Host & Microbe* **28**, 455-
760   464.e452, doi:https://doi.org/10.1016/j.chom.2020.07.005 (2020).
761 47 Schulte-Schrepping, J. *et al.* Severe COVID-19 Is Marked by a Dysregulated Myeloid Cell
762   Compartment. *Cell* **182**, 1419-1440.e1423, doi:10.1016/j.cell.2020.08.001 (2020).
763 48 Brundin-Mather, R. *et al.* Secondary EMR data for quality improvement and research: A
764   comparison of manual and electronic data collection from an integrated critical care electronic
765   medical record system. *J Crit Care* **47**, 295-301, doi:10.1016/j.jcrc.2018.07.021 (2018).
766 49 Cox, J. & Mann, M. MaxQuant enables high peptide identification rates, individualized p.p.b.-
767   range mass accuracies and proteome-wide protein quantification. *Nat Biotechnol* **26**, 1367-
768   1372, doi:10.1038/nbt.1511 (2008).
769 50 Cox, J. *et al.* Andromeda: a peptide search engine integrated into the MaxQuant environment. *J
770   Proteome Res* **10**, 1794-1805, doi:10.1021/pr101065j (2011).
771 51 Huang, T. *et al.* MSstatsTMT: Statistical Detection of Differentially Abundant Proteins in
772   Experiments with Isobaric Labeling and Multiple Mixtures. *Mol Cell Proteomics* **19**, 1706-1723,
773   doi:10.1074/mcp.RA120.002105 (2020).
774 52 Schindelin, J. *et al.* Fiji: an open-source platform for biological-image analysis. *Nature Methods* **9**,
775   676-682, doi:10.1038/nmeth.2019 (2012).
776 53 Zheng, G. X. Y. *et al.* Massively parallel digital transcriptional profiling of single cells. *Nature
777   Communications* **8**, 14049, doi:10.1038/ncomms14049 (2017).
778 54 Stuart, T. *et al.* Comprehensive Integration of Single-Cell Data. *Cell* **177**, 1888-1902.e1821,
779   doi:https://doi.org/10.1016/j.cell.2019.05.031 (2019).
780 55 Hao, Y. *et al.* Integrated analysis of multimodal single-cell data. *bioRxiv*, 2020.2010.2012.335331,
781   doi:10.1101/2020.10.12.335331 (2020).
782 56 Zilionis, R. *et al.* Single-Cell Transcriptomics of Human and Mouse Lung Cancers Reveals
783   Conserved Myeloid Populations across Individuals and Species. *Immunity* **50**, 1317-1334.e1310,
784   doi:https://doi.org/10.1016/j.immuni.2019.03.009 (2019).
785 57 Aran, D. *et al.* Reference-based analysis of lung single-cell sequencing reveals a transitional
786   profibrotic macrophage. *Nature Immunology* **20**, 163-172, doi:10.1038/s41590-018-0276-y
787   (2019).
788 58 Reusch, N. *et al.* Neutrophils in COVID-19. *Frontiers in immunology* **12**, 652470-652470,
789   doi:10.3389/fimmu.2021.652470 (2021).

790 59   Shaath, H., Vishnubalaji, R., Elkord, E. & Alajez, N. M. Single-Cell Transcriptome Analysis
791   Highlights a Role for Neutrophils and Inflammatory Macrophages in the Pathogenesis of Severe
792   COVID-19. *Cells* **9**, doi:10.3390/cells9112374 (2020).
793 60   Schlenner, S. M. *et al.* Fate Mapping Reveals Separate Origins of T Cells and Myeloid Lineages in
794   the Thymus. *Immunity* **32**, 426-436, doi:https://doi.org/10.1016/j.immuni.2010.03.005 (2010).
795 61   Bates, D., Mächler, M., Bolker, B. & Walker, S. Fitting Linear Mixed-Effects Models Using lme4.
796   *Journal of Statistical Software; Vol 1, Issue 1 (2015)*, doi:10.18637/jss.v067.i01 (2015).
797 62   Raredon, M. S. B. *et al.* Connectome: computation and visualization of cell-cell
798   signaling topologies in single-cell systems data. *bioRxiv*, 2021.2001.2021.427529,
799   doi:10.1101/2021.01.21.427529 (2021).
800 63   Jin, S. *et al.* Inference and analysis of cell-cell communication using CellChat. *Nature*
801   *Communications* **12**, 1088, doi:10.1038/s41467-021-21246-9 (2021).
802 64   Alquicira-Hernandez, J. & Powell, J. E. Nebulosa recovers single-cell gene expression signals by
803   kernel density estimation. *Bioinformatics*, doi:10.1093/bioinformatics/btab003 (2021).
804 65   Hafemeister, C. & Satija, R. Normalization and variance stabilization of single-cell RNA-seq data
805   using regularized negative binomial regression. *Genome Biology* **20**, 296, doi:10.1186/s13059-
806   019-1874-1 (2019).
807 66   Janky, R. s. *et al.* iRegulon: From a Gene List to a Gene Regulatory Network Using Large Motif
808   and Track Collections. *PLOS Computational Biology* **10**, e1003731,
809   doi:10.1371/journal.pcbi.1003731 (2014).

810